nature materials

Review article

https://doi.org/10.1038/s41563-023-01492-6

Coherent antiferromagnetic spintronics

Received: 1 July 2022

Accepted: 25 January 2023

Published online: 20 March 2023

Check for updates

Jiahao Han [1] ✉, Ran Cheng [2,3], Luqiao Liu [4], Hideo Ohno [1,5,6,7] & Shunsuke Fukami [1,5,6,7,8] ✉

Antiferromagnets have attracted extensive interest as a material platform in spintronics. So far, antiferromagnet-enabled spin–orbitronics, spin-transfer electronics and spin caloritronics have formed the bases of antiferromagnetic spintronics. Spin transport and manipulation based on coherent antiferromagnetic dynamics have recently emerged, pushing the developing field of antiferromagnetic spintronics towards a new stage distinguished by the features of spin coherence. In this Review, we categorize and analyse the critical effects that harness the coherence of antiferromagnets for spintronic applications, including spin pumping from monochromatic antiferromagnetic magnons, spin transmission via phase-correlated antiferromagnetic magnons, electrically induced spin rotation and ultrafast spin–orbit effects in antiferromagnets. We also discuss future opportunities in research and applications stimulated by the principles, materials and phenomena of coherent antiferromagnetic spintronics.

Spintronics has demonstrated remarkable potential in next-generation memory and computing technologies[1,2]. Owing to the easily accessible magnetic order, ferromagnets became a natural material platform to construct functional devices with prominent spintronic effects. Magnetic tunnel junctions[3], as a representative spintronic device, store binary information 1/0 using the parallel/antiparallel magnetic orientations of two ferromagnetic electrodes, which can be electrically probed by the tunnelling magnetoresistance[3] and switched by the spin-transfer torque[4] or the spin–orbit torque[5] (SOT), corresponding to the reading and writing operations. This enables magnetic random-access memory with remarkable properties, such as non-volatility, long endurance and low power consumption compared with its semiconductor-based counterparts[1,2]. On the other hand, coherent excitations of ferromagnetic order generate spin waves with timescales and wavelengths down to sub-nanoseconds and sub-micrometres, respectively, holding promise for the miniaturization of microwave processing circuits and the design of wave-based computing devices[6].

Unlike ferromagnets, which play active roles in spintronic devices, antiferromagnets had been largely ignored due to their vanishing magnetization and insensitivity to magnetic fields, posing fundamental challenges for probing and manipulating the antiferromagnetic (AFM) order[7,8]. For a long time antiferromagnets only worked as passive ingredients in magnetic tunnel junctions by pinning adjacent ferromagnets[8]. This situation changed drastically after the discoveries of crucial spin–orbit effects in antiferromagnets, including (tunnelling) anisotropic magnetoresistance[9,10] and SOT-induced manipulation of magnetic order[11], which can serve as the reading and writing mechanisms of antiferromagnet-based memory. Owing to this functionalization, spintronic devices based on antiferromagnets benefit from the lack of stray fields, thereby avoiding cross-talk, and good immunity against magnetic perturbations[7]. Meanwhile, the exploration of SOT and magnetoresistance effects in polycrystalline antiferromagnets has made them more compatible with the current Si-based electronics[12,13]. Studies investigating the electrical generation of spin current[14–16] and spin transfer via incoherent magnons[17–19] provided further insights

[1]Research Institute of Electrical Communication, Tohoku University, Sendai, Japan. [2]Department of Electrical and Computer Engineering, University of California Riverside, Riverside, CA, USA. [3]Department of Physics and Astronomy, University of California Riverside, Riverside, CA, USA. [4]Department of Electrical Engineering and Computer Science, Massachusetts Institute of Technology, Cambridge, MA, USA. [5]Center for Science and Innovation in Spintronics, Tohoku University, Sendai, Japan. [6]Center for Innovative Integrated Electronic Systems, Tohoku University, Sendai, Japan. [7]WPI-Advanced Institute for Materials Research, Tohoku University, Sendai, Japan. [8]Inamori Research Institute of Science, Kyoto, Japan. ✉e-mail: jiahao.han.c8@tohoku.ac.jp; s-fukami@riec.tohoku.ac.jp

https://doi.org/10.1038/s41563-023-01492-6

Table 1 | Spin structures of some representative antiferromagnets

Spin structure category	Crystal and spin structure	Magnetic anisotropy	Order parameter	Additional notes
Collinear	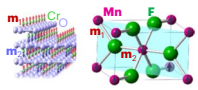	Easy axis [0001] in Cr_2O_3 (left) [001] in MnF_2 (right)	$\mathbf{m}_1$, $\mathbf{m}_2$; or $\mathbf{n}=(\mathbf{m}_2-\mathbf{m}_1)/2$, $\mathbf{m}=(\mathbf{m}_2+\mathbf{m}_1)/2$	In the spin-flop phase, **m** is induced by the applied magnetic field.
	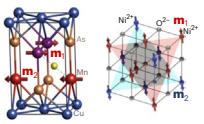	Easy plane (001) in CuMnAs (left) (111) in NiO (right)	$\mathbf{m}_1$, $\mathbf{m}_2$; or $\mathbf{n}=(\mathbf{m}_2-\mathbf{m}_1)/2$, $\mathbf{m}=(\mathbf{m}_2+\mathbf{m}_1)/2$	(1) Also referred as biaxial anisotropy. (2) In the spin-flop phase, **m** is induced by the applied magnetic field (not discussed in this Review).
	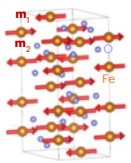	Easy plane (canted) (0001) in α-Fe_2O_3 above the Morin transition	$\mathbf{m}_1$, $\mathbf{m}_2$; or $\mathbf{n}=(\mathbf{m}_2-\mathbf{m}_1)/2$, $\mathbf{m}=(\mathbf{m}_2+\mathbf{m}_1)/2$	(1) The DMI induces **m**. (2) α-Fe_2O_3 exhibits an easy-axis phase (sublattice moments collinear with [0001]) below the Morin transition (not discussed in this Review).
Non-collinear	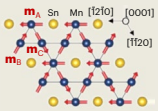	Easy plane (0001) in Mn_3Sn	$\mathbf{m}_A$, $\mathbf{m}_B$, $\mathbf{m}_C$	$\mathbf{m}=(\mathbf{m}_A+\mathbf{m}_B+\mathbf{m}_C)/3$ is induced by the DMI and the magnetic anisotropy.

Crystal and spin structures adapted with permission from (left to right, top to bottom): ref. [106], Elsevier; ref. [40], APS; ref. [11], AAAS; ref. [97], Springer Nature Ltd; ref. [77], APS; ref. [70], Japan Society of Applied Physics.

into AFM spin transport. The above progresses have been the major driving force of AFM spintronics.

Another critical topic is spintronic effects pertaining to the coherent dynamics of AFM order. The dynamics of antiferromagnets is determined by the strong exchange interaction and the magnetic anisotropy, which introduce striking phenomena distinct from their ferromagnetic counterparts. In the past few years, a series of spintronic effects originating from coherent AFM dynamics have been discovered, revealing an emerging frontier of coherent AFM spintronics that could lead to ultrafast, wave-based signal processing technologies. In the following we will introduce the fundamental spin structures and the unique dynamics in antiferromagnets, discuss the remarkable progress in coherent AFM spintronics and provide an outlook on future research and applications.

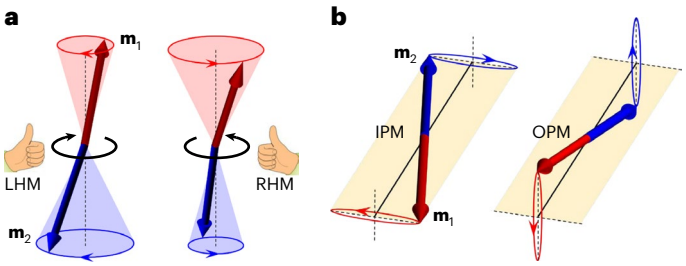

Fig. 1 | Illustration of magnon eigenmodes (uniform modes with zero wavenumber) in collinear antiferromagnets. a, The circularly polarized LHM and RHM in an easy-axis antiferromagnet. **b**, The linearly polarized IPM and OPM in an easy-plane antiferromagnet.

Spin structures and magnon modes in antiferromagnets

Antiferromagnets possess magnetic sublattices with different orientations of magnetic moments. As the simplest configuration, a collinear antiferromagnet is usually described by two antiparallel magnetic sublattices, with magnetic moment directions labelled as $\mathbf{m}_1$ and $\mathbf{m}_2$ as well as a Néel vector $\mathbf{n} = (\mathbf{m}_2 - \mathbf{m}_1)/2$. According to the preferred orientation of **n** (either along a crystallographic axis or within a crystallographic plane), collinear antiferromagnets can exhibit easy-axis and easy-plane anisotropy. In the presence of symmetry breaking factors such as the spin-flop transition, an applied magnetic field, and the Dzyaloshinskii–Moriya interaction (DMI), $\mathbf{m}_1$ and $\mathbf{m}_2$ can be slightly canted[8], resulting in a weak net moment $\mathbf{m} = (\mathbf{m}_2 + \mathbf{m}_1)/2$ perpendicular to **n**. There is another family of antiferromagnets with non-collinear magnetic sublattices, in which at least three vectors $\mathbf{m}_A$, $\mathbf{m}_B$ and $\mathbf{m}_C$ are needed to specify the spin structure[20]. We categorize the antiferromagnets to be discussed in this Review according to these features in Table 1.

The most common form of elementary excitations in ordered magnetic systems is the spin wave (known as a magnon in quantum descriptions)—that is, the oscillation of local magnetic moments around their equilibrium orientations. Unlike ferromagnetic magnons that always have right-handed chirality and carry finite spin angular momenta reducing the ground-state ordering, antiferromagnets exhibit more complicated magnon modes. In easy-axis collinear antiferromagnets, $\mathbf{m}_1$ and $\mathbf{m}_2$ (as well as **n**) undergo circular precessions with either left-handed or right-handed chirality[21] (Fig. 1a). Such left-handed modes (LHMs) and right-handed modes (RHMs) carry finite but opposite spin angular momenta along the easy axis and are degenerate in the absence of external magnetic field[21]. In contrast, easy-plane collinear antiferromagnets exhibit two non-degenerate magnon eigenmodes even at zero magnetic field (Fig. 1b). The in-plane mode (IPM) comes with a lower frequency, in which $\mathbf{m}_1$ and $\mathbf{m}_2$ undergo highly elliptical precessions with opposite chirality and their long axes lie in the easy plane[22,23], leading to a linear precession in **n** that carries vanishing spin on average[24–26]. A similar picture applies to the out-of-plane mode (OPM) that comes with a higher frequency, except that the long axis of the precession trajectory is perpendicular to the easy plane[22,23]. Such IPMs and OPMs are often referred to as linearly polarized modes[24,27,28]. When the sublattice moments are slightly canted and a weak net moment **m** is induced, the main features of the magnon eigenmodes described above are not

https://doi.org/10.1038/s41563-023-01492-6

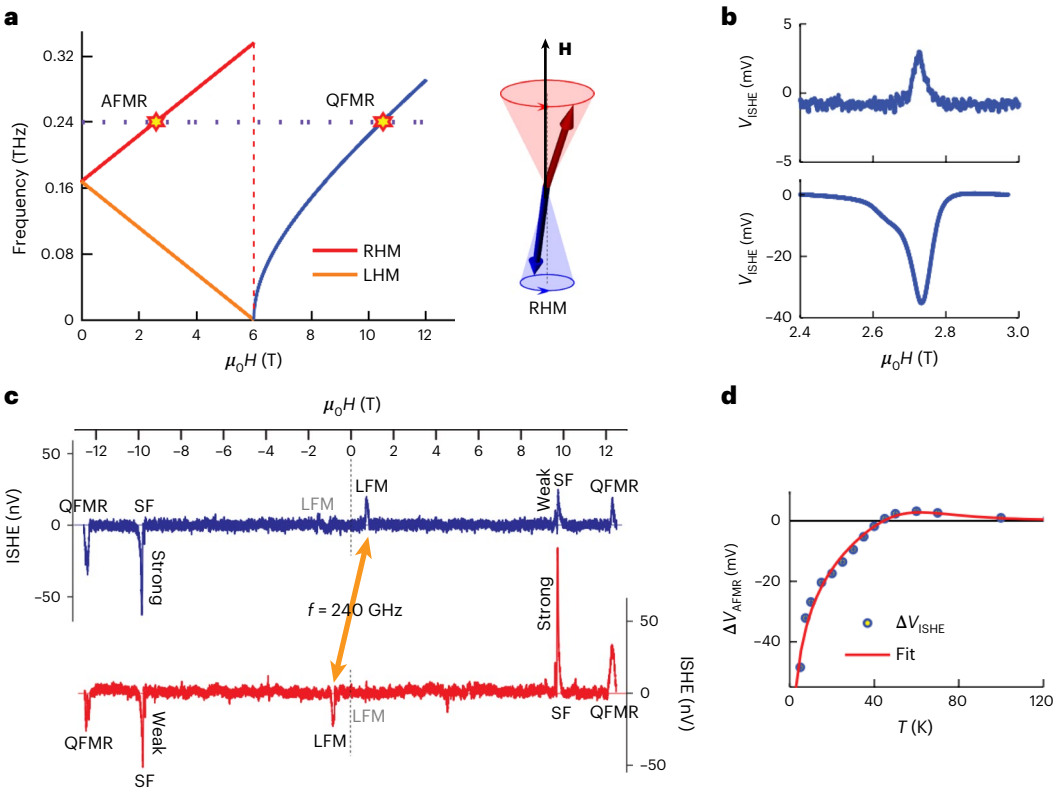

Fig. 2 | Spin pumping from sub-terahertz AFM magnons. a, Eigen frequency versus the applied magnetic field H of uniform-mode (zero wavenumber) magnons in Cr_2O_3. The positive direction of the magnetic field is defined in the inset schematic of the RHM. **b**, Spin pumping signal in Cr_2O_3/Pt (top) and Cr_2O_3/Ta (bottom). Under a positive magnetic field, only the RHM is excited on resonance. **c**, Spin pumping signal in MnF_2/Pt. The blue and red curves correspond to the measurements under left-handed and right-handed microwaves, which excite the LHM and the RHM on resonance, respectively. **d**, Magnitude of the spin pumping from Cr_2O_3 as a function of temperature T. μ_0, vacuum permeability; f, microwave frequency; AFMR, AFM resonance; QFMR, quasi-ferromagnetic resonance; ISHE, inverse spin Hall effect; SF, spin-flop. Panels reproduced with permission from: **a**,**b**,**d**, ref. [34], Springer Nature Limited; **c**, ref. [35], AAAS.

affected qualitatively, except that the oscillation of **m** becomes elliptical[23,29]. The dynamics of non-collinear antiferromagnets goes beyond the simple picture of Fig. 1 and will be discussed in the 'Electrically induced coherent spin rotation in antiferromagnets' section.

Spin pumping from monochromatic AFM magnons

As a critical effect that illustrates how coherent magnons interact with electrons to generate spin currents, spin pumping was identified in ferromagnet/heavy metal bilayers[30–32]. Monochromatic, in-phase magnons induced by the ferromagnetic resonance can transfer spin angular momenta to the electrons in the heavy metal, generating a spin current that flows along the film normal and is subsequently converted into a charge current via the inverse spin Hall effect. In easy-axis antiferromagnets, a similar phenomenon was proposed whereby a spin current $\mathbf{J}_s$ can be generated coherently from the circularly polarized magnons at the AFM resonance, expressed as $\mathbf{J}_s = G_r(\mathbf{n}\times\dot{\mathbf{n}} + \mathbf{m}\times\dot{\mathbf{m}}) - G_i\dot{\mathbf{m}}$, where G_r and G_i are the real and imaginary parts of the interfacial spin-mixing conductance, and the dot over **n** and **m** denotes the time derivative[33]. While the first two terms both contribute to the d.c. component of $\mathbf{J}_s$ (refs. [34,35]), the $\mathbf{n}\times\dot{\mathbf{n}}$ term makes the major contribution[35], where the polarity of $\dot{\mathbf{n}}$ reflects the chirality of the magnon (LHM or RHM) and determines the sign of $\mathbf{J}_s$.

Spin pumping at the AFM resonance has been experimentally demonstrated recently in the insulating easy-axis antiferromagnets Cr_2O_3 and MnF_2 (refs. [34,35]). In the former, a linearly polarized microwave at 0.24 THz was applied to Cr_2O_3/Pt (or Ta) and the inverse spin Hall voltage V_{ISHE} was measured under an applied magnetic field along the easy axis[34]. When the applied field is below the spin-flop threshold, the Néel vector **n** is along the easy axis at equilibrium, while the frequencies of the two circularly polarized magnon modes (LHM and RHM) split linearly with the field strength (Fig. 2a). Consequently, only the RHM (LHM) is excited on resonance under the corresponding positive (negative) field. A finite V_{ISHE} appears at the AFM resonance and exhibits different signs in Cr_2O_3/Pt and Cr_2O_3/Ta (Fig. 2b), which is consistent with the opposite spin Hall angles of Pt and Ta. MnF_2/Pt was also employed for the spin pumping measurement[35], in a similar configuration to that in ref. [34]. The main difference is that the driving microwave has changeable frequencies and is circularly polarized with a switchable chirality, allowing selective excitation of the on-resonance LHM and RHM in MnF_2 when the microwave frequency matches the magnon eigen frequency under an applied magnetic field. As a result, a finite V_{ISHE} is detected, which comes solely from either the LHM or the RHM (Fig. 2c).

A critical question associated with the spin pumping experiments is whether the observed spin current stems from the microwave-driven coherent magnons or from the thermally driven incoherent magnons, as the microwave radiation and the magnetic resonance can cause extra thermal excitations[36–38]. In ferromagnet-based devices, the contributions from coherent and incoherent magnons can be convoluted because they both own right-handed chirality[34,38]. Owing to the selective excitation of LHMs and RHMs by the microwave, antiferromagnets make it possible to exclusively investigate the coherent magnons. In the study on Cr_2O_3 (ref. [34]), under a positive magnetic field, the microwave coherently excites the RHM, while the thermal magnons prefer the LHM due to the lower frequency. The competition between the coherent RHM and the incoherent LHM leads to a sign

change in V_{ISHE} versus temperature (Fig. 2d). As the spin-dependent thermal contribution decays rapidly with increasing temperature (under fixed thermal power)[39], the sign of V_{ISHE} is consistent with the RHM in the high-temperature regime, verifying the existence of spin pumping from coherent AFM magnons. In the study on MnF_2 (ref. [35]), under a circularly polarized microwave that exclusively drives either the LHM or the RHM, the coherent spin pumping origin is corroborated by comparing the sign of V_{ISHE} with the microwave chirality (Fig. 2c). This measurement unambiguously excludes the thermal magnons induced by the microwave heating because thermal excitations should not have such a prominent dependence on the microwave chirality.

We now summarize the existing mechanisms of spin current generation via AFM magnons in addition to the coherent spin pumping. First we look at the spin Seebeck effect that produces a flow of thermal magnons along a temperature gradient[17,40–42]. As discussed above (Fig. 2a), magnon modes in an easy-axis antiferromagnet are circularly polarized and split linearly with a magnetic field along the easy axis until the spin-flop threshold. This picture holds even for magnons of finite wavenumbers[43]. Consequently, under a positive field, the left-handed branch of magnons has lower frequencies than the right-handed branch, being more energetically favourable according to the Bose–Einstein distribution[34,41] and thus determining the sign of the spin Seebeck voltage. In easy-plane antiferromagnets with a vanishing net moment, the spin Seebeck signal may have more complicated origins, among which a possible factor is the dynamics of the surface magnetic atoms[42]. When the applied field is above the spin-flop transition, a net moment **m** is induced at thermal equilibrium, which undergoes right-handed precession upon thermal agitation and gives rise to a spin Seebeck voltage[17,40]. Moreover, in the spin-flop phase, microwaves can drive a coherent, right-handed oscillation of **m** (that is, quasi-ferromagnetic resonance), which also generates a V_{ISHE} signal[34,35]. This **m**-induced spin pumping resembles that from ferromagnets. A similar effect has been observed using a canted antiferromagnet, easy-plane α-Fe_2O_3, where **m** is induced by the DMI of α-Fe_2O_3 without the need for a strong external field[29,44]. The critical role of the oscillation chirality has been further verified by comparing the spin pumping from the left-handed oscillation of the Néel vector in an easy-axis antiferromagnet, the right-handed oscillation of the DMI-induced **m** in a canted antiferromagnet and the conventional right-handed oscillation in a ferromagnet[44]. As expected, the first scenario has an opposite sign in the spin pumping signal compared with the other two.

To make AFM spin pumping useful from a practical perspective, the first question is whether it can be achieved at room temperature. In existing studies, the operating temperature was restricted to <150 K, because of either the low Néel temperature of the material[35] or possible magnon scattering at elevated temperatures[34]. In this regard, a comprehensive study on the temperature dependence of coherent AFM magnons in room-temperature materials is needed. Concerning the functionalization of antiferromagnet-based devices, the spin pumping can potentially be utilized to detect external terahertz radiation[45] and to probe coherent magnon signals transmitted in an AFM channel, the latter of which will play a major role in terahertz wave-based computing (see further discussion in the 'Outlook' section).

Spin transmission via phase-correlated AFM magnons

The coherence of AFM magnons can give rise to various interesting effects in spin transmission. A seminal experiment on the AFM spin transmission was performed using a non-local device geometry, where a pair of isolated Pt electrodes were fabricated as the spin injector and detector on an insulating easy-axis antiferromagnet[19] (Fig. 3a). A charge current in the Pt injector injects spin into the antiferromagnet via the spin Hall effect, which populates one of the two modes (the LHM or RHM) with a broadband spectrum when the injected spin has a collinear component with the Néel vector of the antiferromagnet. These non-equilibrium magnons can convey finite spin over several micrometres, which is detected as V_{ISHE} at the Pt detector[19]. This long-distance spin transmission in easy-axis antiferromagnets can be viewed as a natural consequence of the circularly polarized magnon eigenmodes that carry finite spin. However, the magnon spin transmission in easy-plane antiferromagnets is much more non-trivial, as the linearly polarized IPM and OPM do not individually carry spin. Indeed, it was commonly thought that antiferromagnets with a well-defined easy-plane order are less likely to transmit spin over a long distance[24,39,46,47].

This conventional scheme has recently been challenged by the experimental observation of long-distance magnon spin transmission in the collinear easy-plane antiferromagnet α-Fe_2O_3. By using the non-local device geometry in Fig. 3a, magnon spin transmission over a few micrometres has been detected in highly epitaxial films of α-Fe_2O_3 (ref. [27]). The transmission reaches its maximum when the Néel vector is collinear with the injected spin (Fig. 3b), confirming the AFM nature (that is, the Néel vector oscillation, rather than the dynamics of any net moment) of the observed signal. Coincident effects have also been acquired in the α-Fe_2O_3 bulk material[28]. These two studies[27,28] propose consistent mechanisms to unveil the rich physics of a seemingly impossible effect. The injected spin establishes a phase correlation[26,48] between the two eigenmodes of the IPM and OPM with the same frequency, which are superimposed to form an effective circularly polarized mode carrying finite spin (Fig. 3c). Owing to the unequal wavenumbers of the IPM and the OPM under a fixed frequency (the difference in wavenumber is defined as Δk, which decreases with the frequency according to the magnon dispersion relation[27,28,39]), an IPM–OPM pair keeps interfering during propagation, accompanied by a dephasing. Thus, the spin of the effective magnon mode gradually decays[27,28]. This propagation process of two orthogonally polarized magnons can be intuitively interpreted as an analogy to the birefringence effect in optics. The overall spin decay length λ should be an ensemble average of all non-equilibrium magnons weighted by the Bose–Einstein distribution. As the temperature increases, higher-frequency magnons (with smaller Δk) become more prominent. The interfering magnon pairs experience slower dephasing, which would lead to an increasing λ with temperature[27]. This trend contrasts with the behaviour of the intrinsic circularly polarized magnons in ferromagnets[49–51] and antiferromagnets[28,52], serving as a characteristic feature of the phase-correlated IPM–OPM pairs. This speculation is consistent with the experiment, where the measured λ increases with temperature up to 225 K (Fig. 3d). At even higher temperatures, magnon scattering becomes dominant and results in a shorter λ. Quantitative agreement on the temperature and magnetic field dependences of the magnon spin transmission has been obtained between the experiments and the phenomenological models[27,28].

The concept of the phase-correlated magnon pair can be generalized to induce more striking effects. For example, a pseudospin vector **S** associated with the magnon modes in easy-plane α-Fe_2O_3 has been introduced[53,54]. As shown in Fig. 3e, the precession of **S** accompanies the magnon propagation. It leads to an evolution of the effective magnon mode from right-handed circular to linear to left-handed circular to linear, corresponding to a carrier of positive, zero, negative and zero spin, respectively (the terms of positive and negative are relative to the injected spin from Pt). The precession of **S** shares common physics with the evolution of the phase correlation in the IPM–OPM pair (that is, the spatial accumulation of Δk), while a comprehensive theory that quantitatively cooperates the time evolution of **S** and the spatial evolution of Δk is still pending[47]. By controlling the precession frequency of **S** via an applied magnetic field (Fig. 3f), a Hanle effect has been observed in the magnon spin transmission signal[53]—that is, an oscillation of the signal polarity when the applied magnetic field increases from 0 to 15 T (Fig. 3g). The availability of strong magnetic fields makes the transition of positive signals into the negative region

https://doi.org/10.1038/s41563-023-01492-6

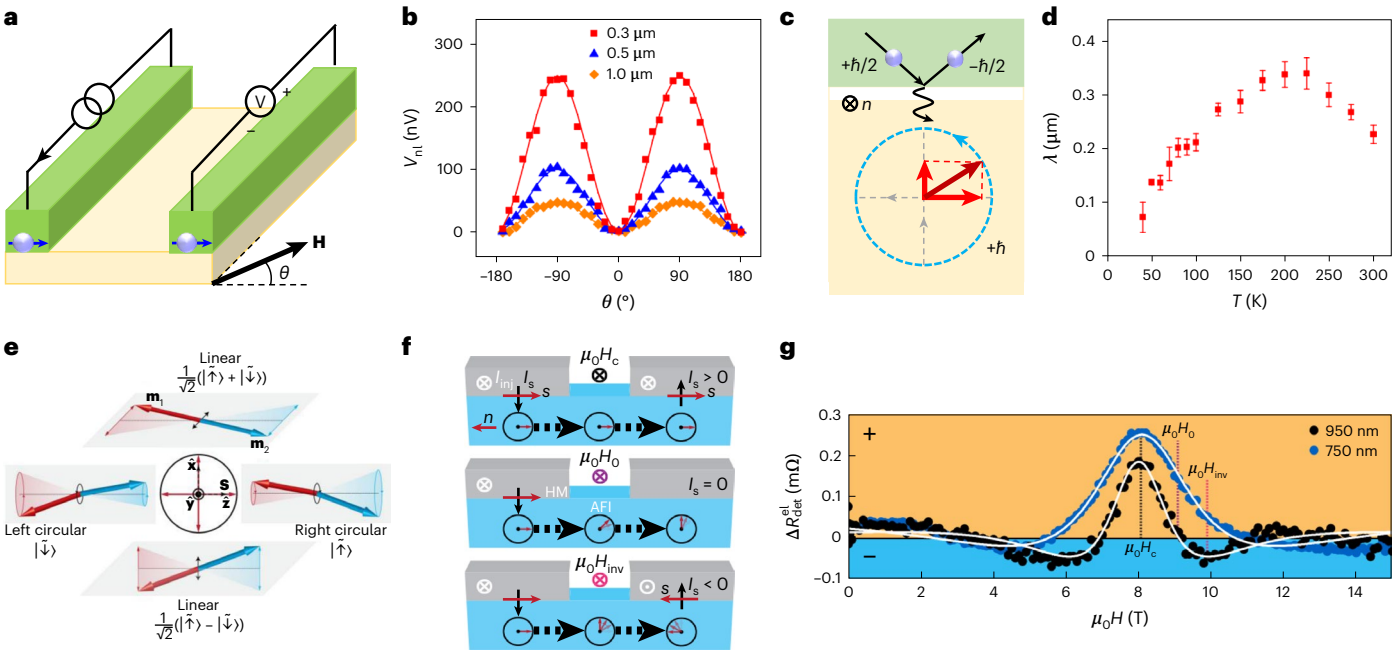

Fig. 3 | Spin transmission via phase-correlated AFM magnons and magnon pseudospin dynamics in easy-plane α-Fe_2O_3. a, Non-local device geometry to measure the magnon spin transmission under an in-plane magnetic field **H**, the angle of which from the horizontal direction is defined as θ. **b**, Magnon spin transmission signal with injector-detector distances of 0.3 μm, 0.5 μm and 1.0 μm at room temperature. **c**, Schematic of the construction of an effective circularly polarized magnon mode (blue dashed line) via a phase-correlated IPM–OPM pair (grey dashed line, which is simplified and shown as linear for clearer illustration). The red arrows represent the oscillating components of the magnetic moments. We note that the DMI of α-Fe_2O_3 does not change the main features of the IPM and OPM[23,26]. **d**, Temperature dependence of the magnon spin decay length. The error bars represent the standard error of the mean from the fitting. **e**, Pseudospin **S** description of AFM magnons. **f**, Magnon spin transmission with **S** precessing in different frequencies, controlled by an applied magnetic field. From top to bottom: under a magnetic field of H_c, H_0 or H_{inv}, a positive, zero or negative magnon spin signal is detected. I_{inj}, injected charge current; I_s, spin current; HM, heavy metal; AFI, AFM insulator. **g**, Magnon spin transmission signal ΔR_{det}^{el} as a function of the applied magnetic field with injector-detector distances of 950 nm and 750 nm. The background shading in orange and blue corresponds to the positive and negative signal, respectively. Panels reproduced with permission from: **b**,**d**, ref. [27], Springer Nature Limited; **e**–**g**, ref. [53], APS.

possible. The periodic sign-flip is particularly intriguing, as it reflects coherent control of the pseudospin dynamics and can be used to design wave-based computing devices.

In these studies, although magnons induced by the spin Hall effect are broadband and seem to transport diffusively[27,28,53], the phase correlation of the magnon pair, as well as the pseudospin model, indicates the indispensable role of coherence for the long-distance magnon spin transmission in easy-plane antiferromagnets. Hence, the effects discussed here are distinct from those in easy-axis antiferromagnets[19] and ferromagnets[55], where the magnons are purely incoherent and phase-uncorrelated. A fundamental question that follows is how the phase correlation of the magnon pair is established. In the existing models[27,28], it is primarily attributed to the magnon excitation mechanism via the spin Hall effect. To absorb the electrically injected spin, two linearly polarized modes with the same frequency should be phase-locked to form an effective circularly polarized mode. We note that the idea of inducing coherence between originally incoherent (quasi-)particles is crucial for many important condensed-matter effects, such as the Cooper pair in superconductors. In this sense, a comprehensive theory on the formation of phase-correlated magnon pairs is desirable.

Furthermore, it is essential to expand the category of material candidates for future studies. So far, among the easy-plane antiferromagnets, only α-Fe_2O_3 and $YFeO_3$ (ref. [56]) have enabled micrometre-scale magnon spin transmission, whereas that in NiO is limited to several nanometres[57–59]. A possible reason is that NiO has a much larger gap between the IPM and the OPM in the magnon dispersion relation than α-Fe_2O_3. The magnon pairs in NiO thus experience faster dephasing and stronger scattering during propagation[27]. When searching for potential materials, a low magnetic damping is desirable, which is crucial to enable long-distance transmission[28] and other quantum effects, such as the AFM cavity magnon polariton[60]. Besides the search for new materials, alternative designs for the device structure can lead to advanced functionality. For example, vertical magnon spin valves allow one to explore magnon spin transmission across an insulating AFM thin film[61–63], providing extra freedom through thickness and interface engineering. It is thus possible to construct a thin-film interferometer operated by the coherence of AFM magnons. The high-density integration of devices can also benefit from a vertical device geometry.

Electrically induced coherent spin rotation in antiferromagnets

The interplay between electrical current and ferromagnetic dynamics led to the innovation of the spin-torque nano-oscillator[64], in which the current-induced spin torque compensates the magnetic damping of a mono-domain ferromagnet and induces a coherent auto-oscillation of the magnetization vector around its equilibrium axis. These studies provide a promising approach to generating microwaves via d.c. current, while the small cone angle of the magnetic oscillation (usually a few degrees[64]) results in moderate magnetic and electrical responses. It is highly desirable that magnetic moments can precess with a much larger amplitude. Recently, coherent rotation of the whole spin structure driven by the SOT, with the precession cone angle approaching 90°, has been demonstrated in antiferromagnets[65,66]. In this section, we will review the key materials, physics and techniques that stimulated these findings.

In general, easy-plane anisotropy is helpful for the large-cone-angle spin rotation in antiferromagnets. A promising material is the

https://doi.org/10.1038/s41563-023-01492-6

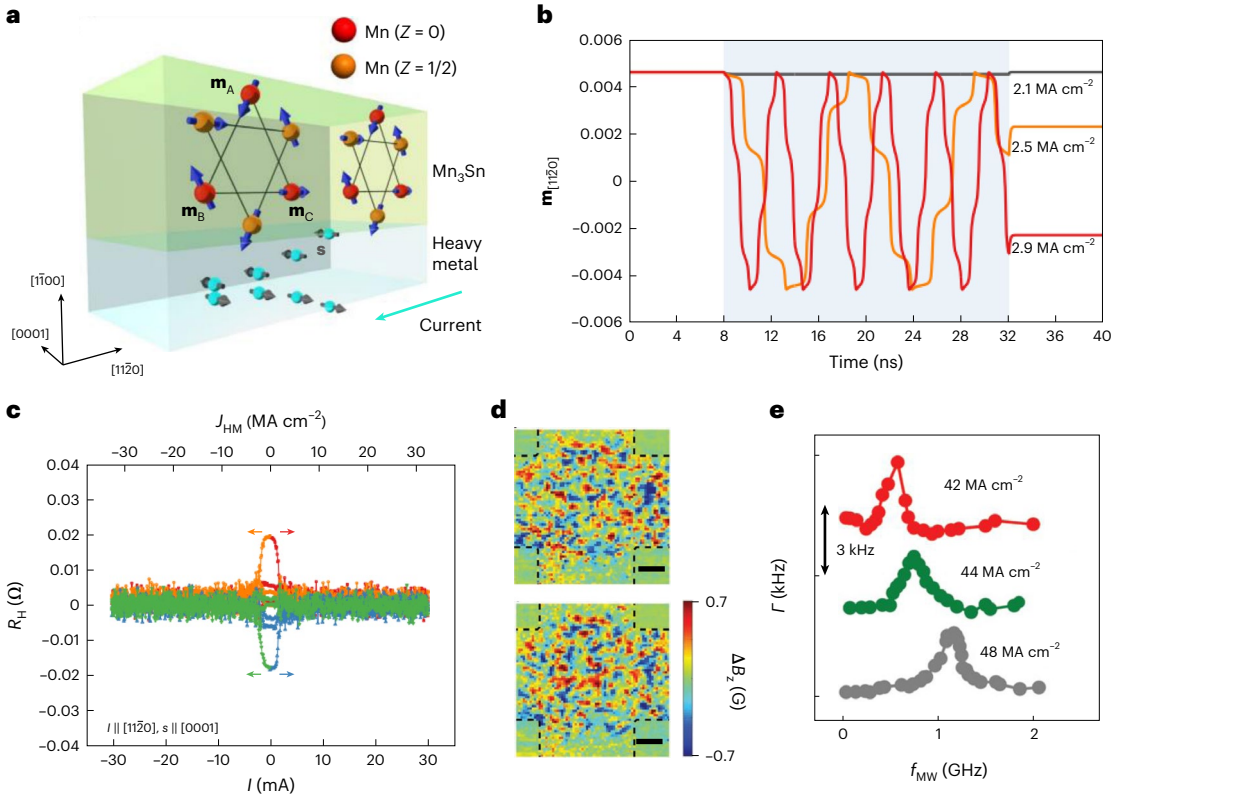

Fig. 4 | SOT-driven coherent chiral-spin rotation in non-collinear antiferromagnet Mn_3Sn. a, Schematic of the Mn_3Sn/heavy metal device. The electrical current injects spin **s** to Mn_3Sn. The kagome planes of Mn_3Sn are perpendicular to **s**. *Z* is the index of the kagome planes. **b**, Calculated chiral-spin rotation under different driving currents, probed by the [11$\bar{2}$0]component of **m**. The shading corresponds to the period in which the driving current is applied. **c**, Fluctuation of R_H induced by current pulses. The arrows denote the current scanning directions of the corresponding plots. **d**, Nitrogen-vacancy centre images of the SOT-induced variation of stray field ΔB_z in a Mn_3Sn/Pt device, recorded after applying current pulses 10 (top) and 20 (bottom) times. Scale bar, 2.5 μm. The dashed lines mark the device edges. **e**, Nitrogen-vacancy relaxation rate Γ as a function of the applied microwave frequency f_{MW} under different driving currents. There is a peak in Γ when f_{MW} matches the intrinsic frequency of the chiral-spin rotation. Panels reproduced with permission from: **a**–**c**, ref. [65], Springer Nature Limited; **d**,**e**, ref. [66], Wiley.

non-collinear antiferromagnet $D0_{19}$-Mn_3X (X = Sn, Ge), where the (0001) kagome plane formed by three Mn sublattices ($\mathbf{m}_A$, $\mathbf{m}_B$ and $\mathbf{m}_C$) is the magnetic easy plane[20,67,68] (Fig. 4a). The magnetic moments form a chiral-spin structure due to the geometrical frustration and the DMI[67,68]. Despite a weak net magnetization on the order of 10 kA m^{-1} (corresponding to a net moment $\mathbf{m} = (\mathbf{m}_A + \mathbf{m}_B + \mathbf{m}_C)/3$), Mn_3X exhibits a large anomalous Hall resistance R_H due to the non-vanishing Berry curvature arising from the topologically non-trivial band structure[20]. R_H can be used to monitor the orientation of the chiral-spin structure marked by the out-of-plane component of **m** (refs. [67–69]).

Owing to the development of highly epitaxial Mn_3Sn films on heavy metal seed layers[70], a device geometry that enables coherent rotation of the chiral-spin structure has been constructed[65] (Fig. 4a). The (0001) kagome planes are perpendicular to the film plane. A driving current generates non-equilibrium spin **s** along [0001] (perpendicular to the kagome plane) via the spin Hall effect of the heavy metal, exerting a damping-like SOT $\boldsymbol{\tau}_\mu^{DL} \propto \mathbf{m}_\mu \times (\mathbf{m}_\mu \times \mathbf{s})$ on each Mn moment $\mathbf{m}_\mu$ (μ = A, B, C). The SOT induces a slight canting of the magnetic moments towards [0001], which breaks the energy balance in the non-collinear ground state and initiates precessional torques arising from the exchange interaction[65,71,72]. When the precessional torques overcome the magnetic anisotropy in the kagome plane, a coherent spin rotation of the three magnetic sublattices is established. This spin rotation leads to an instantaneous (Gilbert) damping torque $\alpha \mathbf{m}_\mu \times \dot{\mathbf{m}}_\mu$ that is exactly compensated by the driving SOT, with α denoting the Gilbert damping coefficient[65,71]. The larger the SOT, the faster the rotation (Fig. 4b). If the driving current switches its polarity, the precessional torques also flip sign and the magnetic moments rotate in the opposite direction. After turning off the driving current, the chiral-spin structure stops rotating and resettles in one of the six stable configurations defined by the six-fold magnetic anisotropy in the kagome plane. This is shown by the observation of fluctuating R_H under pulsed currents (Fig. 4c). We note that although the chiral-spin structure has six stable orientations in a single domain corresponding to six step levels of R_H, the multi-domain structure of the device would cause a transition of R_H into somewhere between the stable levels due to an ensemble average of accommodated domains. This speculation is supported by the experiment, where the fluctuation of R_H becomes smaller as the device expands to contain more domains[65].

Besides transport measurements, the chiral-spin rotation in Mn_3Sn has also been probed via nitrogen-vacancy centre imaging[66], which is sensitive to the local stray field generated by the chiral-spin structure of Mn_3Sn. Figure 4d shows the spatial distribution of stray fields on the surface of a multi-domain Mn_3Sn/Pt device and its evolution with current pulses, which visualizes the reorientation of the chiral-spin structure driven by the SOT from Pt. More strikingly, by continuously applying a driving current and a microwave to effectively synchronize the spin rotation among different domains, a resonant chiral-spin rotation is detected (Fig. 4e). The rotation frequency is ~1 GHz under a driving current density of ~5×10^7 A cm^{-2} and increases with the current. This work provides direct evidence of the coherent and continuous rotation of AFM order driven by electrical approaches. By further

increasing the driving current, it is possible that the rotation frequency could reach a few terahertz[72]. In applications, one could integrate the conductive Mn_3X into magnetic tunnel junctions, where the chiral-spin rotation produces microwave signals via the tunnelling (anisotropic) magnetoresistance effect[72,73].

We note that the damping-like SOT can apply to various antiferromagnets, not limited to the non-collinear ones. Indeed, it has been formulated in earlier studies of switching collinear antiferromagnets[74,75]. While thermal effects can influence the switching results[76,77], subsequent studies have verified the essential role of SOT[12,78,79]. In non-collinear antiferromagnets, SOT-induced phenomena may also be modulated by the accompanied thermal effects. In the chiral-spin rotation, Joule heating should not play a major role in causing the oscillating signal, as is shown by a strong dependence of the threshold current on the crystal orientation[65] and the tunable oscillation frequency by the driving current[66]. Meanwhile, it is possible that Joule heating weakens the magnetic anisotropy in the kagome plane and reduces the threshold current. A recent work showed that a combination of SOT and Joule heating can switch a thick Mn_3Sn film by seeding the spin texture from the interface[80]. To gather deeper insights into current-driven AFM dynamics, one can utilize nanodot devices with a single AFM domain to make the chiral-spin rotation more consistent and monochromatic. A combined investigation of the current- and field-induced dynamics could quantify the SOT strength through the measurable magnetic field. This approach has been extensively used with ferromagnets[81], while it requires more sophisticated designs and analysis for measuring antiferromagnets. A determination of the switching/rotation phase diagram[82] can thoroughly reveal the manipulation mechanism.

The mechanism of SOT-driven coherent spin rotation described above was also theoretically studied in simple two-sublattice antiferromagnets[83–85]. For example, in a specially oriented α-Fe_2O_3/Pt bilayer, where the easy plane of α-Fe_2O_3 is tilted from the film plane, the injected spin from Pt can excite the terahertz rotation of the Néel vector, which is accompanied by a precession of the DMI-induced net moment that is amenable to detection[85]. The tilted α-Fe_2O_3/Pt bilayer has been grown and the SOT-induced bipolar switching of the Néel vector was achieved under an applied magnetic field[78]. For both collinear and non-collinear antiferromagnets, if the anisotropy in the easy plane is absent (that is, a perfect easy-plane antiferromagnet), the rotation frequency will grow linearly with the driving current density and the threshold will be effectively zero[65,85]. In real materials, however, due to the finite in-easy-plane anisotropy, the rotation frequency deviates from the linear dependence in the low-current regime[65,66]. Another defining feature of the coherent spin rotation driven by the injected perpendicular-to-easy-plane spin is that the rotation direction is reversible by switching the current polarity, which provides an additional tuning knob for the spin dynamics.

Alternatively, coherent auto-oscillation can be driven by a non-equilibrium spin accumulation $\mathbf{s}$ collinear with the Néel vector that compensates the Gilbert damping[86], which is similar to the ferromagnetic spin-torque nano-oscillator[64] but has a much higher frequency. Different from the aforementioned $\mathbf{s}$-perpendicular-to-easy-plane scenario, the rotation frequency is highly nonlinear with the driving current[86] and the Néel vector precesses around its equilibrium (that is, in the easy-axis direction). Under either mechanism, to achieve a more practical driving current materials with lower damping and weaker in-easy-plane (or in-hard-plane) anisotropy are desirable. Searching for appropriate materials might be challenging, because the low damping can be supported by an ordered crystal structure, but the distinct crystal orientations may lead to strong magnetic anisotropy at the same time. Potential strategies include element doping[47] and strain engineering[78]. Given the theoretical and experimental progress made so far, we are optimistic that an AFM terahertz oscillator is achievable in the future.

Ultrafast spin–orbit and spin-transfer effects in antiferromagnets

The intrinsic frequency of spin dynamics up to terahertz makes antiferromagnets a promising platform to speed up the spin–orbit and spin-transfer effects. The electrical approach to ultrafast switching is open when the terahertz dynamics meets the SOT physics[84,87]. It has been theoretically predicted that a current pulse on the order of 10 ps can coherently reverse the Néel vector via the damping-like SOT[84] (Fig. 5a). The staggered SOT in antiferromagnets with non-centrosymmetric crystal structure, such as CuMnAs (ref. [11]) and Mn_2Au (refs. [87,88]), also holds promise for ultrafast switching. In these materials, opposite spin polarizations $\mathbf{s}_1$ and $\mathbf{s}_2$ (= $-\mathbf{s}_1$) locally act on the sublattice moments $\mathbf{m}_1$ and $\mathbf{m}_2$ (= $-\mathbf{m}_1$), respectively, in the form of the field-like SOT $\boldsymbol{\tau}_{1,2}^{FL} \propto \mathbf{m}_{1,2} \times \mathbf{s}_{1,2}$ to induce cooperative switching of the sublattice moments and hence the Néel vector[87], the timescale of which is on the order of 10 ps (ref. [89]).

The theoretical prediction of ultrafast, coherent switching of antiferromagnets via the SOT triggered a flurry of experimental exploration. In CuMnAs, by alternately applying picosecond electrical pulses that are polarized along two orthogonal directions, reversible switching traces in the Hall resistance have been obtained[90] (Fig. 5b), which is interpreted as a result of the reorientation of the Néel vector via the staggered field-like SOT. The energy density of picosecond switching is comparable to that of microsecond switching in the same material[11] and matches the energy density in ferromagnetic spin-torque devices with gigahertz writing speeds[91,92]. The insulating antiferromagnet α-Fe_2O_3 also enables picosecond control of the Néel vector when adjacent to a heavy metal; in this case the torque responsible for the switching is the damping-like SOT[93]. We note that in these studies the switching effect is probed by the Hall resistance before and after the current pulses, while a time-resolved switching process is yet to be established. Moreover, given the multi-domain feature of the studied antiferromagnets, the switching can be facilitated by SOT-induced motion of AFM domain walls[94].

To verify the role of coherent AFM dynamics in ultrafast SOT switching, one needs to determine the switching time and probe the coherent precession of the Néel vector[95]. A recent experiment showed time-resolved perturbation of AFM order in PtMn and IrMn using the spin-transfer torque from a ferromagnetic spin polarizer[96]. The timescale of the AFM perturbation is a few picoseconds, suggesting the feasibility of realizing coherent switching at terahertz speeds via electrical means. The influence of thermal effects[76,77] also needs to be evaluated in the ultrafast regime. Direct probing of the AFM dynamics via the magneto-optic Faraday or Kerr effect[95,96] is expected to provide independent evidence in addition to the transport effects.

As an inverse effect of controlling magnetic order by picosecond spin torques, the ultrafast generation of spin current via transient magnetic dynamics has been reported in the insulating antiferromagnet NiO paired with a heavy metal[97]. A laser pulse is applied to the sample to trigger the magnetic dynamics of NiO, generating a terahertz emission with a duration of ~1 ps (Fig. 5c). The emission has finite magnitude but opposite polarity in NiO/Pt and NiO/W, and becomes almost negligible in bare NiO and NiO/Cu. This observation is consistent with the scenario of inverse spin Hall effect and thus indicates the transient spin current from NiO. The angular dependence of the terahertz emission has a correspondence to the three-fold symmetry of the NiO crystal around the [111] axis, which provides the possibility of controlling terahertz emission via crystalline symmetry.

Whether the transient spin current arises from the coherent AFM dynamics is of interest. In the NiO device[97], the emission reaches its maximum when the film plane coincides with the magnetic easy plane (111). It seems that the observed terahertz emission is mainly caused by the atomic magnetic moments in the film plane, similar to the configuration of continuous spin pumping[34,35]. However, different from the latter (whose spin current originates from the on-resonance Néel

https://doi.org/10.1038/s41563-023-01492-6

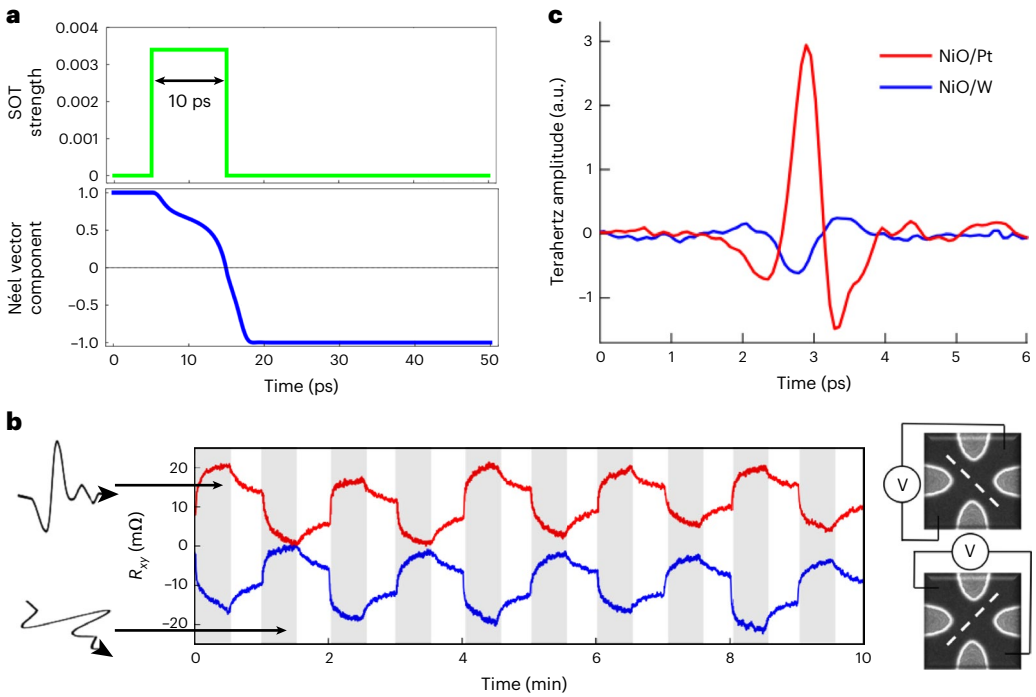

Fig. 5 | Ultrafast SOT switching and spin current generation in antiferromagnets. a, Calculated picosecond switching of the Néel vector in an easy-plane antiferromagnet induced by the SOT. **b**, Reversible multilevel switching of CuMnAs by picosecond electrical pulses. Left: the terahertz electric fields with two orthogonal polarizations are applied alternately in the grey intervals and are turned off in the white intervals. Right: schematic of the Hall resistance readout, where the white dashed lines depict readout current paths. **c**, Terahertz emission from the (111)-NiO/Pt (or NiO/W) samples. Panel **a** adapted with permission from ref. [84], APS. Panels reproduced with permission from: **b**, ref. [90], under a Creative Commons license CC BY-NC 4.0; **c**, ref. [97], Springer Nature Limited.

vector oscillation), the transient spin current in the former is primarily attributed to the dynamics of a net magnetization stemming from the laser-induced impulsive magnetic moment[97], thus exhibiting a broadband spectrum similar to the insulating-ferromagnet-based terahertz emitters[98].

Before closing this section, we recall that theoretical studies demonstrated the feasibility of using coherent AFM dynamics to achieve the ultrafast spin–orbit and spin-transfer effects. Meanwhile, two experimental fingerprints—the temporal evolution of picosecond switching and a narrowband terahertz emission from coherent AFM dynamics—should be thoroughly investigated. From a practical point of view, compared with the existing AFM terahertz emitters that rely on the impulsive magnetic moment, coherent precession of a well-defined Néel vector could in principle generate ultrafast spin current in a more efficient manner. To achieve this goal, one could consider antiferromagnets whose Néel vectors can be manipulated through coherent lattice vibrations. A recent work on the terahertz emission from the coherent AFM magnons induced by the strain wave in NiO may shed light in this direction[99].

Table 2 | Opportunities of coherent AFM spintronics in terahertz devices

Fundamental effect	Device functionality
Spin pumping from monochromatic AFM magnons	Terahertz radiation detectors Terahertz magnonic logic for wave-based computing (detection port)
Spin transmission via phase-correlated AFM magnons	Pseudospin magnonic logic for wave-based computing (lateral) Thin-film interferometer of terahertz magnons (vertical)
Electrically induced coherent spin rotation in antiferromagnets	Tunable spin-torque nano-oscillator (large and small cone angles) Terahertz magnonic logic for wave-based computing (excitation port) Dissipationless, ultrafast transmitter based on AFM spin superfluid
Ultrafast spin–orbit and spin-transfer effects in antiferromagnets	Picosecond coherent switching for AFM random-access memory Terahertz emitter from coherent AFM magnons

Outlook

Owing to the timely exploration of the rich interplay between spin transport and cooperative sublattice spin dynamics, antiferromagnets are ushering in a new intriguing stage in spintronics featuring spin coherence and ultrafast spin dynamics. In particular, several inspiring effects reveal how spin current induces AFM excitations with coherent features (for example, SOT-induced spin rotation, terahertz-speed SOT switching) and vice versa (for example, sub-terahertz spin pumping, spin transmission via phase-correlated magnons, picosecond spin current), providing unique opportunities for building ultrafast memory units, new signal processing devices and terahertz signal generators. Despite a rapidly growing volume of literature, this field is still in its infancy compared with its well-established ferromagnetic counterpart[6]. As a final remark, we propose a few possible directions that may facilitate ongoing studies and fuel the future of coherent AFM spintronics (Table 2).

First, further efforts in materials synthesis are needed to develop thin-film antiferromagnets with more controllable domain patterns. While the AFM domain size in some bulk materials can reach a few tens of micrometres[19,100], the typical domain size of thin films is on the order of 0.1–1 μm (refs. [42,101,102]). The multi-domain structure compromises the coherent excitation of AFM order, for which an extra driving force may be required to synchronize the phase of spin precession[66]. Moreover, it has been shown that the magnetic domain walls can cause extra

magnon scattering and weaken the magnon spin transmission[27,103]. Therefore, a domain size of a few micrometres is necessary to explore the intrinsic and more prominent effects of coherent spin excitation and propagation, which may require a fine tuning of the film uniformity and the interfacial strain[65,70].

Second, despite the realization of spin pumping from uniform magnon modes and the locally SOT-driven spin dynamics, the electrical excitation and detection of propagating spin precession with single frequency and phase resolution[104] remains elusive in antiferromagnets. A demonstration of this effect could provide an analogy to the current-induced ballistic transport of ferromagnetic magnons[32], rendering a more competitive and vibrant field of coherent AFM spintronics. From a practical point of view, an electrically operated device that allows coherent signal transmission is of great importance for wave-based computing[6]. To achieve this goal, one could exploit easy-axis antiferromagnets, in which the coherent magnons can be excited by SOT and detected through spin pumping. We also consider spin transmission via phase-correlated AFM magnons or, more visually, the coherent dynamics of magnon pseudospin, as prospective candidate mechanisms. The magnon pseudospin vector evolving in time and space can be used as a unique information carrier to exploit its wave features. In both cases, the operation speed may benefit from the high velocity of AFM magnons[105]. Furthermore, the electric field control of AFM order[106–108] can be integrated to provide an extra knob for modulating the phase-coherent transport of chiral magnons, which will effectively demonstrate an AFM magnon field-effect transistor[26].

Third, given the theoretical and experimental progress in the picosecond electrical switching of antiferromagnets, it is desirable to explore alternative mechanisms to further optimize the switching efficiency and speed. On the one hand, the switching current can be reduced by using more efficient spin-current generators, such as topological insulators with spin-momentum locked surface states and topological semimetals with spin–orbit-coupled band nodes[109]. Benefiting from these potential spin sources, the spin-injection-induced coherent AFM dynamics can reach the terahertz frequency regime at a lower driving current. On the other hand, as switching enabled by the motion of AFM domain walls has been established[94], the influence of domain walls on the switching speed deserves further investigation. An ultimate question is whether even faster switching can be achieved in the coherent switching of a single-domain antiferromagnet. Given a recent report that 6-ps-wide electrical pulses can switch the magnetization of the common ferromagnet Co via the SOT[110], addressing this enquiry becomes more essential, as picosecond electrical switching no longer seems to be unique to antiferromagnets. We hope that this intriguing open question can inspire more advancements in the ultrafast, coherent switching of antiferromagnets, which will eventually revolutionize the writing speed and the energy efficiency of all-AFM random-access memory.

Last but not least, coherent excitations of AFM order could lead to new phenomena in condensed matter. As an example, spin superfluid was initially proposed as a dissipationless transport of coherent spin precession in ferromagnets with in-plane anisotropy[111], while it was found that the dipolar interaction of ferromagnetic moments may cause a fast decay of the spin supercurrent[112]. Easy-plane antiferromagnets with both collinear[83,113] and non-collinear configurations[114,115] were considered better candidates due to vanishingly small net magnetization. In these proposals, the device structure is similar to Fig. 3a, in which a pair of heavy metal electrodes serves as the spin injector and detector via the spin Hall and the inverse spin Hall effects, respectively. When the spin injected into the antiferromagnet has a perpendicular-to-easy-plane component, the Néel vector will collectively precess about the direction of the injected spin. To achieve this configuration, it is necessary that the easy plane tilts away from the film plane, which has been realized in α-Fe_2O_3 (ref. [78]), NiO (ref. [97]) and Mn_3Sn (refs. [65,70,82]) thin films. Among these candidate materials, weak anisotropy in the easy plane is preferable, which ensures a smooth and continuous precession of the Néel vector. Endowed by a number of theoretical predictions, we look forward to an experimental realization of the spin superfluid in an easy-plane antiferromagnet.

References

1. Bhatti, S. et al. Spintronics based random access memory: a review. *Mater. Today* **20**, 530–548 (2017).
2. Dieny, B. et al. Opportunities and challenges for spintronics in the microelectronics industry. *Nat. Electron.* **3**, 446–459 (2020).
3. Miyazaki, T. & Tezuka, N. Giant magnetic tunneling effect in Fe/Al_2O_3/Fe junction. *J. Magn. Magn. Mater.* **139**, L231–L234 (1995).
4. Huai, Y., Albert, F., Nguyen, P., Pakala, M. & Valet, T. Observation of spin-transfer switching in deep submicron-sized and low-resistance magnetic tunnel junctions. *Appl. Phys. Lett.* **84**, 3118–3120 (2004).
5. Liu, L. et al. Spin-torque switching with the giant spin Hall effect of tantalum. *Science* **336**, 555–558 (2012).
6. Pirro, P., Vasyuchka, V. I., Serga, A. A. & Hillebrands, B. Advances in coherent magnonics. *Nat. Rev. Mater.* **6**, 1114–1135 (2021).
7. Jungwirth, T., Marti, X., Wadley, P. & Wunderlich, J. Antiferromagnetic spintronics. *Nat. Nanotechnol.* **11**, 231–241 (2016).
8. Baltz, V. et al. Antiferromagnetic spintronics. *Rev. Mod. Phys.* **90**, 015005 (2018).
9. Marti, X. et al. Room-temperature antiferromagnetic memory resistor. *Nat. Mater.* **13**, 367–374 (2014).
10. Park, B. G. et al. A spin-valve-like magnetoresistance of an antiferromagnet-based tunnel junction. *Nat. Mater.* **10**, 347–351 (2011).
11. Wadley, P. et al. Electrical switching of an antiferromagnet. *Science* **351**, 587–590 (2016).
12. DuttaGupta, S. et al. Spin-orbit torque switching of an antiferromagnetic metallic heterostructure. *Nat. Commun.* **11**, 5715 (2020).
13. DuttaGupta, S., Itoh, R., Fukami, S. & Ohno, H. Angle dependent magnetoresistance in heterostructures with antiferromagnetic and non-magnetic metals. *Appl. Phys. Lett.* **113**, 202404 (2018).
14. Fukami, S., Zhang, C., DuttaGupta, S., Kurenkov, A. & Ohno, H. Magnetization switching by spin–orbit torque in an antiferromagnet–ferromagnet bilayer system. *Nat. Mater.* **15**, 535–541 (2016).
15. Kimata, M. et al. Magnetic and magnetic inverse spin Hall effects in a non-collinear antiferromagnet. *Nature* **565**, 627–630 (2019).
16. Chen, X. et al. Observation of the antiferromagnetic spin Hall effect. *Nat. Mater.* **20**, 800–804 (2021).
17. Seki, S. et al. Thermal generation of spin current in an antiferromagnet. *Phys. Rev. Lett.* **115**, 266601 (2015).
18. Qiu, Z. et al. Spin colossal magnetoresistance in an antiferromagnetic insulator. *Nat. Mater.* **17**, 577–580 (2018).
19. Lebrun, R. et al. Tunable long-distance spin transport in a crystalline antiferromagnetic iron oxide. *Nature* **561**, 222–225 (2018).
20. Kübler, J. & Felser, C. Non-collinear antiferromagnets and the anomalous Hall effect. *Europhys. Lett.* **108**, 67001 (2014).
21. Keffer, F. & Kittel, C. Theory of antiferromagnetic resonance. *Phys. Rev.* **85**, 329–337 (1952).
22. Sievers, A. J. III & Tinkham, M. Far infrared antiferromagnetic resonance in MnO and NiO. *Phys. Rev.* **129**, 1566–1571 (1963).
23. Williamson, S. J. & Foner, S. Antiferromagnetic resonance in systems with Dzyaloshinsky-Moriya coupling; orientation dependence in αFe_2O_3. *Phys. Rev.* **136**, A1102–A1106 (1964).
24. Gomonay, O., Baltz, V., Brataas, A. & Tserkovnyak, Y. Antiferromagnetic spin textures and dynamics. *Nat. Phys.* **14**, 213–216 (2018).

25. Satoh, T. et al. Spin oscillations in antiferromagnetic NiO triggered by circularly polarized light. *Phys. Rev. Lett.* **105**, 077402 (2010).
26. Cheng, R., Daniels, M. W., Zhu, J.-G. & Xiao, D. Antiferromagnetic spin wave field-effect transistor. *Sci. Rep.* **6**, 24223 (2016).
27. Han, J. et al. Birefringence-like spin transport via linearly polarized antiferromagnetic magnons. *Nat. Nanotechnol.* **15**, 563–568 (2020).
28. Lebrun, R. et al. Long-distance spin-transport across the Morin phase transition up to room temperature in ultra-low damping single crystals of the antiferromagnet α-Fe_2O_3. *Nat. Commun.* **11**, 6332 (2020).
29. Wang, H. et al. Spin pumping of an easy-plane antiferromagnet enhanced by Dzyaloshinskii-Moriya interaction. *Phys. Rev. Lett.* **127**, 117202 (2021).
30. Tserkovnyak, Y., Brataas, A. & Bauer, G. E. W. Enhanced Gilbert damping in thin ferromagnetic films. *Phys. Rev. Lett.* **88**, 117601 (2002).
31. Mizukami, S., Ando, Y. & Miyazaki, T. Effect of spin diffusion on Gilbert damping for a very thin permalloy layer in Cu/permalloy/Cu/Pt films. *Phys. Rev. B* **66**, 104413 (2002).
32. Kajiwara, Y. et al. Transmission of electrical signals by spin-wave interconversion in a magnetic insulator. *Nature* **464**, 262–266 (2010).
33. Cheng, R., Xiao, J., Niu, Q. & Brataas, A. Spin pumping and spin-transfer torques in antiferromagnets. *Phys. Rev. Lett.* **113**, 057601 (2014).
34. Li, J. et al. Spin current from sub-terahertz-generated antiferromagnetic magnons. *Nature* **578**, 70–74 (2020).
35. Vaidya, P. et al. Subterahertz spin pumping from an insulating antiferromagnet. *Science* **368**, 160–165 (2020).
36. Yamanoi, K., Yokotani, Y. & Kimura, T. Dynamical spin injection based on heating effect due to ferromagnetic resonance. *Phys. Rev. Appl.* **8**, 054031 (2017).
37. Cheng, J. et al. Quantitative estimation of thermoelectric contributions in spin pumping signals through microwave photoresistance measurements. *Phys. Rev. B* **103**, 014415 (2021).
38. Chen, Y. S., Lin, J. G., Huang, S. Y. & Chien, C. L. Incoherent spin pumping from YIG single crystals. *Phys. Rev. B* **99**, 220402(R) (2019).
39. Rezende, S. M., Rodríguez-Suárez, R. L. & Azevedo, A. Diffusive magnonic spin transport in antiferromagnetic insulators. *Phys. Rev. B* **93**, 054412 (2016).
40. Wu, S. M. et al. Antiferromagnetic spin Seebeck effect. *Phys. Rev. Lett.* **116**, 097204 (2016).
41. Li, J. et al. Spin Seebeck effect from antiferromagnetic magnons and critical spin fluctuations in epitaxial FeF_2 films. *Phys. Rev. Lett.* **122**, 217204 (2019).
42. Gray, I. et al. Spin Seebeck imaging of spin-torque switching in antiferromagnetic Pt/NiO heterostructure. *Phys. Rev. X* **9**, 041016 (2019).
43. Kefer, F., Kaplan, H. & Yafet, Y. Spin waves in ferromagnetic and antiferromagnetic materials. *Am. J. Phys.* **21**, 250–257 (1953).
44. Boventer, I. et al. Room-temperature antiferromagnetic resonance and inverse spin-Hall voltage in canted antiferromagnets. *Phys. Rev. Lett.* **126**, 187201 (2021).
45. Gomonay, O., Jungwirth, T. & Sinova, J. Narrow-band tunable terahertz detector in antiferromagnets via staggered-field and antidamping torques. *Phys. Rev. B* **98**, 104430 (2018).
46. Khymyn, R., Lisenkov, I., Tiberkevich, V. S., Slavin, A. N. & Ivanov, B. A. Transformation of spin current by antiferromagnetic insulators. *Phys. Rev. B* **93**, 224421 (2016).
47. Ross, A. et al. An insulating doped antiferromagnet with low magnetic symmetry as a room temperature spin conduit. *Appl. Phys. Lett.* **117**, 242405 (2020).
48. Bender, S. A. & Tserkovnyak, Y. Interfacial spin and heat transfer between metals and magnetic insulators. *Phys. Rev. B* **91**, 140402(R) (2015).
49. Guo, E.-J. et al. Influence of thickness and interface on the low-temperature enhancement of the spin Seebeck effect in YIG films. *Phys. Rev. X* **6**, 031012 (2016).
50. Cornelissen, L. J., Shan, J. & van Wees, B. J. Temperature dependence of the magnon spin diffusion length and magnon spin conductivity in the magnetic insulator yttrium iron garnet. *Phys. Rev. B* **94**, 180402(R) (2016).
51. Zhou, X. J. et al. Lateral transport properties of thermally excited magnons in yttrium iron garnet films. *Appl. Phys. Lett.* **110**, 062407 (2017).
52. Gückelhorn, J. et al. Influence of low-energy magnons on magnon Hanle experiments in easy-plane antiferromagnets. *Phys. Rev. B* **105**, 094440 (2022).
53. Wimmer, T. et al. Observation of antiferromagnetic magnon pseudospin dynamics and the Hanle effect. *Phys. Rev. Lett.* **125**, 247204 (2020).
54. Kamra, A., Wimmer, T., Huebl, H. & Althammer, M. Antiferromagnetic magnon pseudospin: dynamics and diffusive transport. *Phys. Rev. B* **102**, 174445 (2020).
55. Cornelissen, L. J., Liu, J., Duine, R. A., Youssef, J. B. & van Wees, B. J. Long-distance transport of magnon spin information in a magnetic insulator at room temperature. *Nat. Phys.* **11**, 1022–1026 (2015).
56. Das, S. et al. Anisotropic long-range spin transport in canted antiferromagnetic orthoferrite $YFeO_3$. *Nat. Commun.* **13**, 6140 (2022).
57. Wang, H., Du, C., Hammel, P. C. & Yang, F. Antiferromagnonic spin transport from $Y_3Fe_5O_{12}$ into NiO. *Phys. Rev. Lett.* **113**, 097202 (2014).
58. Dąbrowski, M. et al. Coherent transfer of spin angular momentum by evanescent spin waves within antiferromagnetic NiO. *Phys. Rev. Lett.* **124**, 217201 (2020).
59. Baldrati, L. et al. Spin transport in multilayer systems with fully epitaxial NiO thin films. *Phys. Rev. B* **98**, 014409 (2018).
60. Boventer, I. et al. Antiferromagnetic cavity magnon polaritons in collinear and canted phases of hematite. *Phys. Rev. Appl.* **19**, 014071 (2023).
61. Cramer, J. et al. Magnon detection using a ferroic collinear multilayer spin valve. *Nat. Commun.* **9**, 1089 (2018).
62. Guo, C. Y. et al. A nonlocal spin Hall magnetoresistance in a platinum layer deposited on a magnon junction. *Nat. Electron.* **3**, 304–308 (2020).
63. Zhou, Y. et al. Orthogonal interlayer coupling in an all-antiferromagnetic junction. *Nat. Commun.* **13**, 3723 (2022).
64. Kiselev, S. I. et al. Microwave oscillations of a nanomagnet driven by a spin-polarized current. *Nature* **425**, 380–383 (2003).
65. Takeuchi, Y. et al. Chiral-spin rotation of non-collinear antiferromagnet by spin–orbit torque. *Nat. Mater.* **20**, 1364–1370 (2021).
66. Yan, G. Q. et al. Quantum sensing and imaging of spin-orbit-torque-driven spin dynamics in noncollinear antiferromagnet Mn_3Sn. *Adv. Mater.* **34**, 2200327 (2022).
67. Nakatsuji, S., Kiyohara, N. & Higo, T. Large anomalous Hall effect in a non-collinear antiferromagnet at room temperature. *Nature* **527**, 212–215 (2015).
68. Nayak, A. K. et al. Large anomalous Hall effect driven by a nonvanishing Berry curvature in the noncolinear antiferromagnet Mn_3Ge. *Sci. Adv.* **2**, e1501870 (2016).
69. Tsai, H. et al. Electrical manipulation of a topological antiferromagnetic state. *Nature* **580**, 608–613 (2020).
70. Yoon, J. et al. Crystal orientation and anomalous Hall effect of sputter-deposited non-collinear antiferromagnetic Mn_3Sn thin films. *Appl. Phys. Express* **13**, 013001 (2020).
71. Yamane, Y., Gomonay, O. & Sinova, J. Dynamics of noncollinear antiferromagnetic textures driven by spin current injection. *Phys. Rev. B* **100**, 054415 (2019).

72. Shukla, A. & Rakheja, S. Spin-torque-driven terahertz auto-oscillations in noncollinear coplanar antiferromagnets. *Phys. Rev. Appl.* **17**, 034037 (2022).
73. Dong, J. et al. Tunneling magnetoresistance in noncollinear antiferromagnetic tunnel junctions. *Phys. Rev. Lett.* **128**, 197201 (2022).
74. Moriyama, T. et al. Spin torque control of antiferromagnetic moments in NiO. *Sci. Rep.* **8**, 14167 (2018).
75. Chen, X. Z. et al. Antidamping-torque-induced switching in biaxial antiferromagnetic insulators. *Phys. Rev. Lett.* **120**, 207204 (2018).
76. Chiang, C. C. et al. Absence of evidence of electrical switching of the antiferromagnetic Néel vector. *Phys. Rev. Lett.* **123**, 227203 (2019).
77. Zhang, P. et al. Quantitative study on current-induced effect in an antiferromagnet insulator/Pt bilayer film. *Phys. Rev. Lett.* **123**, 247206 (2019).
78. Zhang, P. et al. Control of Néel vector with spin-orbit torques in an antiferromagnetic insulator with tilted easy plane. *Phys. Rev. Lett.* **129**, 017203 (2022).
79. Chen, X. et al. Control of spin current and antiferromagnetic moments via topological surface state. *Nat. Electron.* **5**, 574–578 (2022).
80. Pal, B. et al. Setting of the magnetic structure of chiral kagome antiferromagnets by a seeded spin-orbit torque. *Sci. Adv.* **8**, eabo5930 (2022).
81. Han, J. & Liu, L. Topological insulators for efficient spin-orbit torques. *APL Mater.* **9**, 060901 (2021).
82. Higo, T. et al. Perpendicular full switching of chiral antiferromagnetic order by current. *Nature* **607**, 474–479 (2022).
83. Takei, S., Halperin, B. I., Yacoby, A. & Tserkovnyak, Y. Superfluid spin transport through antiferromagnetic insulators. *Phys. Rev. B* **90**, 094408 (2014).
84. Cheng, R., Daniels, M. W., Zhu, J.-G. & Xiao, D. Ultrafast switching of antiferromagnets via spin-transfer torque. *Phys. Rev. B* **91**, 064423 (2015).
85. Sulymenko, O. R. et al. Terahertz-frequency spin Hall auto-oscillator based on a canted antiferromagnet. *Phys. Rev. Appl.* **8**, 064007 (2017).
86. Cheng, R., Xiao, D. & Brataas, A. Terahertz antiferromagnetic spin Hall nano-oscillator. *Phys. Rev. Lett.* **116**, 207603 (2016).
87. Železný, J. et al. Relativistic Néel-order fields induced by electrical current in antiferromagnets. *Phys. Rev. Lett.* **113**, 157201 (2014).
88. Bodnar, S. Y. et al. Writing and reading antiferromagnetic Mn_2Au by Néel spin-orbit torques and large anisotropic magnetoresistance. *Nat. Commun.* **9**, 348 (2018).
89. Roy, P. E., Otxoa, R. M. & Wunderlich, J. Robust picosecond writing of a layered antiferromagnet by staggered spin-orbit fields. *Phys. Rev. B* **94**, 014439 (2016).
90. Olejník, K. et al. Terahertz electrical writing speed in an antiferromagnetic memory. *Sci. Adv.* **4**, eaar3566 (2018).
91. Bedau, D. et al. Spin-transfer pulse switching: from the dynamic to the thermally activated regime. *Appl. Phys. Lett.* **97**, 262502 (2010).
92. Baumgartner, M. et al. Spatially and time-resolved magnetization dynamics driven by spin–orbit torques. *Nat. Nanotechnol.* **12**, 980–986 (2017).
93. Huang, L. et al. Terahertz pulse-induced Néel vector switching in α-Fe_2O_3/Pt heterostructures. *Appl. Phys. Lett.* **119**, 212401 (2021).
94. Wadley, P. et al. Current polarity-dependent manipulation of antiferromagnetic domains. *Nat. Nanotechnol.* **13**, 362–365 (2018).
95. Schlauderer, S. et al. Temporal and spectral fingerprints of ultrafast all-coherent spin switching. *Nature* **569**, 383–387 (2019).
96. Kang, K., Lee, W.-B., Lee, D.-K., Lee, K.-J. & Choi, G.-M. Magnetization dynamics of antiferromagnetic metals of PtMn and IrMn driven by a pulsed spin-transfer torque. *Appl. Phys. Lett.* **118**, 252407 (2021).
97. Qiu, H. et al. Ultrafast spin current generated from an antiferromagnet. *Nat. Phys.* **17**, 388–394 (2021).
98. Wu, W., Yaw Ameyaw, C., Doty, M. F. & Jungfleisch, M. B. Principles of spintronic THz emitters. *J. Appl. Phys.* **130**, 091101 (2021).
99. Rongione, E. et al. Emission of coherent THz magnons in an antiferromagnetic insulator triggered by ultrafast spin-phonon interactions. Preprint at https://arxiv.org/abs/2205.11965 (2022).
100. Higo, T. et al. Large magneto-optical Kerr effect and imaging of magnetic octupole domains in an antiferromagnetic metal. *Nat. Photon.* **12**, 73–78 (2018).
101. Grzybowski, M. J. et al. Imaging current-induced switching of antiferromagnetic domains in CuMnAs. *Phys. Rev. Lett.* **118**, 057701 (2017).
102. Uchimura, T. et al. Observation of domain structure in non-collinear antiferromagnetic Mn_3Sn thin films by magneto-optical Kerr effect. *Appl. Phys. Lett.* **120**, 172405 (2022).
103. Ross, A. et al. Propagation length of antiferromagnetic magnons governed by domain configurations. *Nano Lett.* **20**, 306–313 (2020).
104. Hortensius, J. R. et al. Coherent spin-wave transport in an antiferromagnet. *Nat. Phys.* **17**, 1001–1006 (2021).
105. Lee, K. et al. Superluminal-like magnon propagation in antiferromagnetic NiO at nanoscale distances. *Nat. Nanotechnol.* **16**, 1337–1341 (2021).
106. Wang, J.-L., Echtenkamp, W., Mahmood, A. & Binek, C. Voltage controlled magnetism in Cr_2O_3 based all-thin-film systems. *J. Magn. Magn. Mater.* **486**, 165262 (2019).
107. Yan, H. et al. A piezoelectric, strain-controlled antiferromagnetic memory insensitive to magnetic fields. *Nat. Nanotechnol.* **14**, 131–136 (2019).
108. Chen, X. et al. Electric field control of Néel spin–orbit torque in an antiferromagnet. *Nat. Mater.* **18**, 931–935 (2019).
109. Narang, P., Garcia, C. A. C. & Felser, C. The topology of electronic band structures. *Nat. Mater.* **20**, 293–300 (2021).
110. Jhuria, K. et al. Spin–orbit torque switching of a ferromagnet with picosecond electrical pulses. *Nat. Electron.* **3**, 680–686 (2020).
111. Takei, S. & Tserkovnyak, Y. Superfluid spin transport through easy-plane ferromagnetic insulators. *Phys. Rev. Lett.* **112**, 227201 (2014).
112. Skarsvåg, H., Holmqvist, C. & Brataas, A. Spin superfluidity and long-range transport in thin-film ferromagnets. *Phys. Rev. Lett.* **115**, 237201 (2015).
113. Qaiumzadeh, A., Skarsvåg, H., Holmqvist, C. & Brataas, A. Spin superfluidity in biaxial antiferromagnetic insulators. *Phys. Rev. Lett.* **118**, 137201 (2017).
114. Li, B. & Kovalev, A. A. Spin superfluidity in noncollinear antiferromagnets. *Phys. Rev. B* **103**, L060406 (2021).
115. Goli, V. M. L. D. P. & Manchon, A. Crossover from diffusive to superfluid transport in frustrated magnets. *Phys. Rev. B* **103**, 104425 (2021).

Acknowledgements

S.F. acknowledges funding from JSPS Kakenhi grant numbers 19H05622 and 22F32037, MEXT Initiative to Establish Next-generation Novel Integrated Circuits Centers (X-NICS) grant number JPJ011438 and the Cooperative Research Projects of the RIEC. R.C. is supported by the US Air Force Office of Scientific Research grant number FA9550-19-1-0307. L.L. acknowledges support from the US National Science Foundation grant number DMR-2104912. J.H. acknowledges support from the JSPS Postdoctoral Fellowship for Research in Japan.

Author contributions

J.H. and S.F. proposed the topic and main aspects of the paper. All authors participated in writing and discussions.

Competing interests

The authors declare no competing interests.

Additional information

Correspondence should be addressed to Jiahao Han or Shunsuke Fukami.

Peer review information *Nature Materials* thanks Romain Lebrun and the other, anonymous, reviewer(s) for their contribution to the peer review of this work.